Applied Surface Science 604 (2022) 154557

Contents lists available at ScienceDirect

Applied Surface Science

journal homepage: www.elsevier.com/locate/apsusc

Full Length Article

Synchrotron EXAFS spectroscopy and density functional theory studies of Pd/MoS_2 Schottky-type nano/hetero-junctions

A. Taherkhani, S.Z. Mortazavi *, S. Ahmadi, A. Reyhani

Physics Dept, Faculty of Science, Imam Khomeini International University, P.O. Box 34149-16818 Qazvin, Iran

ARTICLE INFO

Keywords:
Pd/MoS_2 Schottky-type nano/hetero-junctions
Extended X-ray absorption fine structure
Thermal chemical deposition vapor deposition
DC magnetron sputtering
Quantum ESPRESSO software

ABSTRACT

Molybdenum disulfide (MoS_2) nanostructures are grown on the silicon substrates using thermal chemical vapor deposition and then Pd anchoring on them is carried out by DC magnetron sputtering to form Pd/MoS_2 Schottky-type nano/hetero-junctions. Extended X-ray absorption fine structure (EXAFS) spectroscopy is applied to study the local structure around the molybdenum K-edge. In this way, the kind, coordination number, and distance of neighbors of absorber atom are determined. Moreover, structural analysis has been performed by X-ray diffraction. Optical studies are conducted by UV–Visible and differential reflectance spectroscopy. The electronic properties of the samples are examined using Raman spectroscopy with an excitation laser at 532 nm. Furthermore, the surface chemical analysis is monitored by X-ray photoelectron spectroscopy. In addition, a simulation study of the structural and electronical properties of the samples is carried out to understand the effect of Pd adding on MoS_2 structure using Quantum ESPRESSO software. The reasonable place of the Pd atom after Pd anchoring in MoS_2 lattice is obtained.

1. Introduction

Semiconducting layered transition-metal dichalcogenides (TMDCs) are gaining more interest due to the possibility of tuning the band-gaps which are used in various applications such as transistor technology, solar cell & photovoltaics, photocatalysis, solid lubricants, and opto-electronics [1–8]. These structures are expressed as MX_2 (M = Mo, W, Ta, Ti, Nb, etc.; X = S, Se, Te) in which a hexagonal layer of M metal atoms is sandwiched between two layers of X chalcogen atoms [9]. Molybdenum disulfide (MoS_2) is the most common TMDC, consisting of several phases i.e., the hexagonal 2H form, which is predominant for bulk MoS_2, whereas monolayer ones have 1H and metastable 1 T polytypes. When 1H-MoS_2 layers are stacked one by one, hexagonal 2H and rhombohedral 3R phases can be formed [10,11]. In hexagonal structure, the arrangement of Mo and S atoms stacked together by weak Van-der-Waals forces to form S–Mo–S sandwiches coordinated in a triangular prismatic fashion [12–15]. MoS_2 semiconductor, as a typical representative of the TMDs family, has attracted more consideration owing to its narrow band-gap and high charge mobility ratio at room temperature [16]. MoS_2 is an *n*-type semiconductor, due to S vacancies [17], with a tunable band-gap with an indirect-to-direct transition from about 1.1 to 1.97 eV from bulk to monolayers, respectively [18,19]. This versatile optical transition enhances photoluminescence property that has found potential applications in high-performance logic devices, integrated circuits, optoelectronics, ultrafast lasers, memristors, optical sensors, photocatalysis, and hydrogen evolution [20–28]. Generally, these compounds can be obtained by different techniques such as physical vapor deposition (PVD), chemical vapor deposition (CVD), and sulfurization methods [29–31].

On the other hand, the fabrication of heterostructures assembled with semiconductors and noble metals gold (Au), silver (Ag), platinum (Pt), etc., is a useful strategy for engineering and improving optical properties [32,33]. The noble metal nanoparticles anchored on the semiconducting materials would enhance the optical properties of the heterostructures based on the interfacial electron transfer mechanism (Schottky junction), which is often considered a potential technological solution in modern photonics [34–36]. Two-dimensional (2D) semiconductors are considered to be excellent channel materials for future electronic and optoelectronic devices due to excellent gate electrostatics in atomically thin crystals, reduced interface traps at dangling-bond-free surfaces, and high carrier mobility in flat layer structures [37]. So, the fabrication of these heterostructures made with metals such as gold (Au), silver (Ag), platinum (Pt), and palladium (Pd) and semiconductors is one of the useful strategies for improving optical and electronical

* Corresponding author.
E-mail address: z.mortazavi@sci.ikiu.ac.ir (S.Z. Mortazavi).

https://doi.org/10.1016/j.apsusc.2022.154557
Received 11 April 2022; Received in revised form 21 July 2022; Accepted 11 August 2022
Available online 17 August 2022

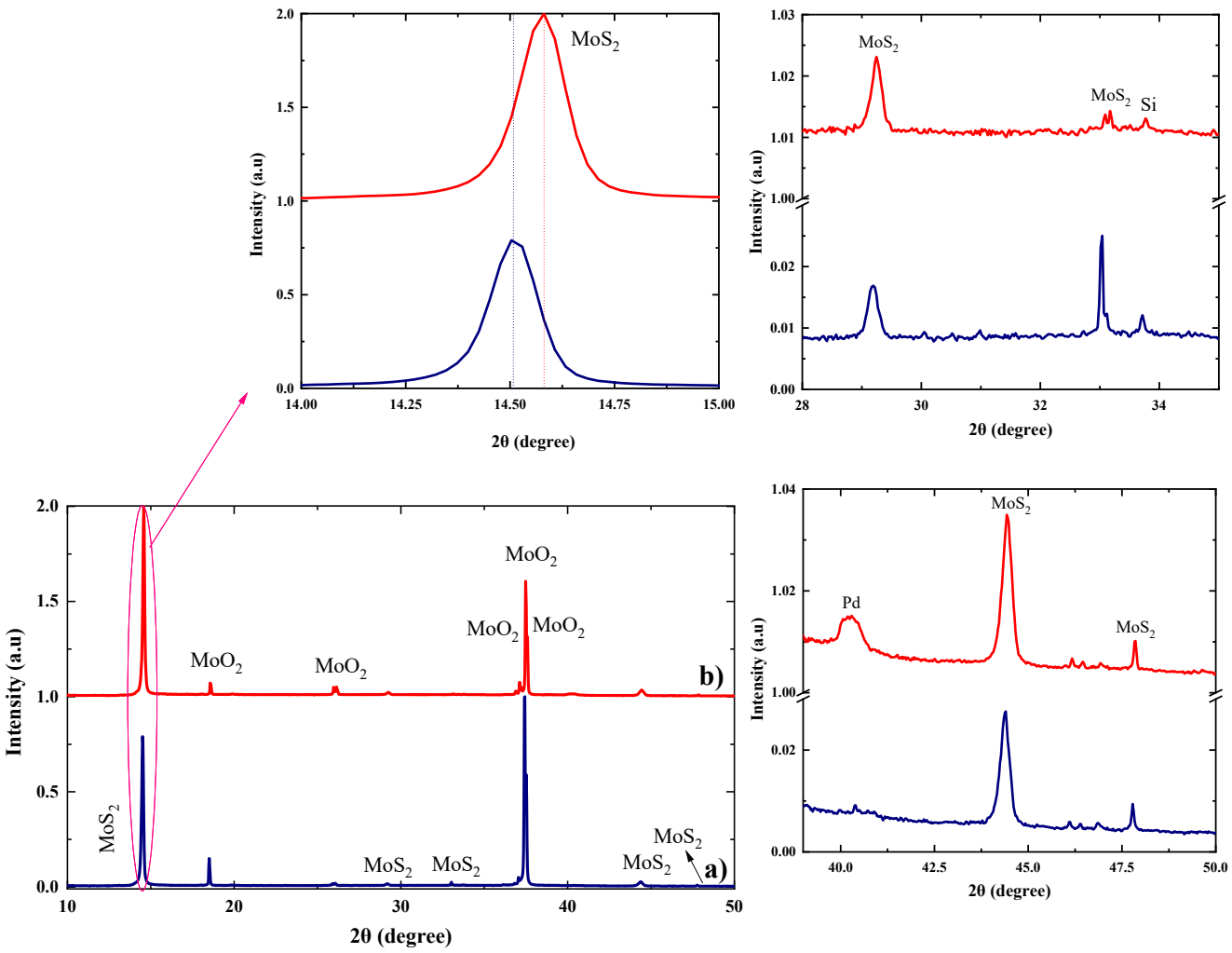

Fig. 1. X-ray diffraction patterns of a) pristine-MoS_2 NSs and b) Pd/MoS_2 NHs.

properties of the semiconductors [32,37].

In this study, firstly, MoS_2 nanostructures (NSs) are grown on SiO_2 buffered p-type silicon substrates via one-step thermal chemical vapor deposition (TCVD) through simultaneous evaporation of the precursors in each process. After that, Pd/MoS_2 Schottky-type nano/hetero-junctions (NHs) are fabricated using DC magnetron sputtering technique. Then, the obtained layers are characterized using X-ray diffraction (XRD), UV–Visible, diffuse reflectance (DRS), Raman, and X-ray photoelectron spectroscopy (XPS). Moreover, X-ray absorption fine structure spectroscopy (XAFS) is applied to study the structural properties of these heterostructures. This work aims to investigate the coordination environment of absorber atom (Mo) in the nano-heterostructures. The molybdenum K-edge is investigated to find the local structure of Mo and study the effect of Pd metal anchoring on the MoS_2 NSs. Extended X-ray absorption fine structure (EXAFS) is an element-specific spectroscopy technique that demonstrates high sensitivity to the local structural changes around the absorbing atom, including the number of neighbors and bond distances, and also the type of them. EXAFS spectroscopy is related to the environment around any absorbing atom, mainly up to 6 Å corresponding to 1–3 coordination shells [38].

On the other hand, a systematic theoretical study is useful to realize and explore the wide range of applications for nanoscale electronics and spintronic devices based on MoS_2 modified by noble metals i.e., Pd atoms [39]. However, several experimental and simulation studies investigated the structural properties and the effect of transition metal decorated on TMDCs structures [40–42], but a few of them studied local structure around the absorber atom. In this research, the diffusion of Pd elements in MoS_2 ML is studied by using density functional theory (DFT) to perform ab initio calculations on the electronic properties of Pd/MoS_2 NHs using Quantum ESPRESSO software.

2. Experimental materials and methods

At first, P-type silicon (1 0 0) chip wafers with single side polished as substrates with 2 cm × 2 cm dimension were used for the fabrication of MoS_2 NSs and Pd/MoS_2 NHs. Before the deposition process, the substrates were cleaned and degreased sequentially with acetone, ethanol, and deionized water for 10 min at 30 °C separately in an ultrasonic bath. Then, the cleaned substrates were immersed in 10 percent hydrofluoric acid (HF ~ 10 %) for a few seconds to eliminate the natural oxidation from the silicon surface. Then, the substrates were dried in an atmosphere oven for 5 min at 80 °C. Subsequently, a silicon oxide insulating buffer layer was produced through a thermal oxidation process in the horizontal tubular furnace (TF5/25–1250). Then, to grow MoS_2 NSs, the substrate was placed inside a ceramic boat loaded in the quartz tubular furnace at atmospheric pressure. Accordingly, the MoO_3 powder (60 mg) and sulfur powder (2100 mg) were situated separately in the ceramic crucibles. One of them contain MoO_3 powder which was placed at the center of the tube at 1000 °C (high temperature) and the SiO_2/Si substrate was placed face down on top of the MoO_3 powder. The other one was allocated to sulfur powder, located adequately far from the first

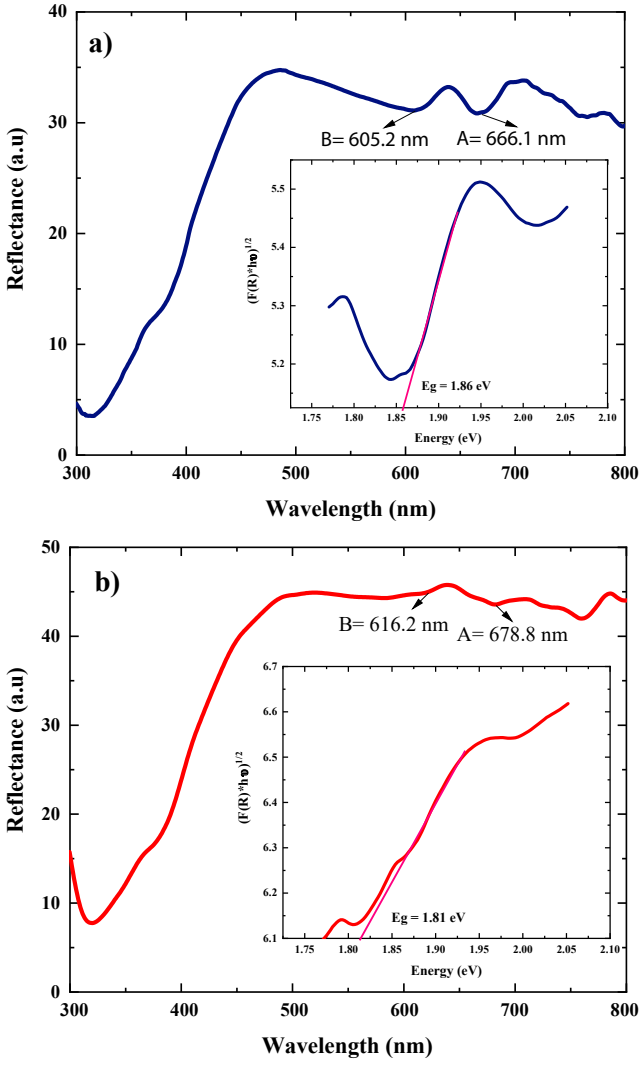

Fig. 2. Diffuse reflectance spectra for a) pristine-MoS_2 NSs and b) Pd/MoS_2 NHs in the wavelength range of 300–800 nm and band gap determination of the samples from the $(F(R)\cdot h\nu)^{1/2}$ vs energy plots.

Table 1
A and B excitons position and band gap values calculated by Kubelka-Munk equation of diffuse reflectance spectra of the samples.

Sample	A exciton position (nm)	B exciton position (nm)	Band gap (Eg) (eV)
pristine-MoS_2 NSs	666.1	605.2	1.86
Pd/MoS_2 NHs	678.8	616.2	1.81

crucible at 200 °C (low-temperature zone) near the gas inlet. It is worth noting that simultaneous sublimation of the precursors is critical to achieving an optimal condition. Thus, the long distance between the positions provides appropriate conditions. Before heating the furnace, the tube was purged by Ar gas at a flow rate of 450 sccm for 30 min to remove another gas from the furnace. Then, the furnace temperature was gradually increased up to 1000 °C in 30 min and then kept invariant at the temperature for one hour in Ar flow rate of 200 sccm. Finally, the furnace was switched off allowing it to cool down by natural convection to reach room temperature again. To deposit Pd on the synthesized MoS_2 NSs, a DC magnetron sputtering (Nanostructured Coatings Co.DST3, Iran) was employed. The Pd NSs were deposited under monomeric pressure 2.3 × 10^{-2} mbar at room temperature with a 42 sccm Ar gas

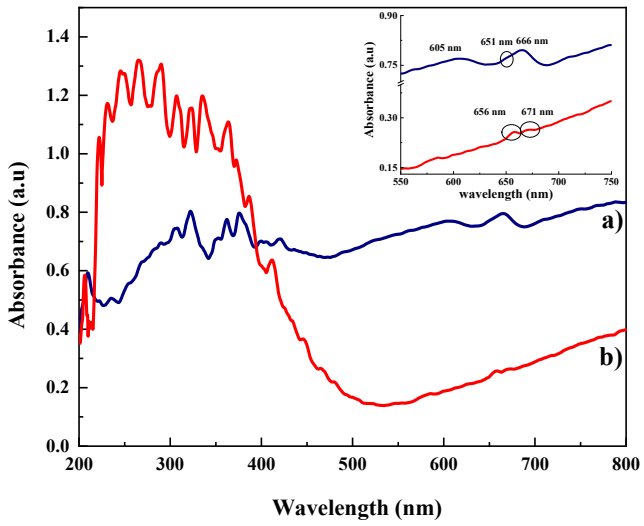

Fig. 3. Absorbance spectra for a) pristine-MoS_2 NSs and b) Pd/MoS_2 NHs in the wavelength range of 200–800 nm.

flow rate. During the experiments, the applied current and voltage are set to be 300 V and 0.03 A, respectively.

The crystalline structure of the grown layers was characterized by an X-ray diffractometer, X'Pert PRO MPD PANalytical, using Cu Kα radiation at λ = 1.54 Å. Optical reflectance of samples and estimating their bandgap were studied using a Scinco (Instrument Serial No.: S4100-00-0701001U) diffuse reflection spectroscopy (DRS). In addition, UV–Visible absorption spectroscopy was performed using a Stellat Net EEP spectrometer. Raman spectroscopy was carried out to study the electronic properties of the samples with an excitation laser at 532 nm. X-ray photoelectron spectroscopy (XPS) (model: BESTEC (EA 10)) was used to gain further insight into the chemical composition of the MoS_2 NSs before and after Pd anchoring. Furthermore, the local atomic structure around the Mo atom was studied by EXAFS spectroscopy with the spectra collected at the BL22 CLÆSS beamline at the ALBA light source (Barcelona, Spain) at the K-edge of Mo (E = 20000 eV). Spectra were taken in Fluorescence mode using a fluorescence solid-state Silicon Drift detector. The synchrotron radiation emitted by a multipole wiggler was first vertically collimated and then monochromatized by a Si (3 1 1) double-crystal monochromator. For the theoretical EXAFS calculations, the Fourier transform was performed in the k^3 χ(k) weighted EXAFS signal between 2.5 and 11.0 $Å^{-1}$ at the Mo K-edge. Experimental EXAFS results were fitted in R-space using the FEFF code.

3. Result and discussion

Fig. 1 demonstrates XRD patterns taken from pristine-MoS_2 NSs and Pd/MoS_2 NHs. The peaks corresponding to MoS_2 structures attributed to 003, 006, 101, 009 and 107 crystalline planes appear in both samples at 2θ = 14.50°, 29.19°, 33.03°, 44.34° and 47.78° and it confirms formation the rhombohedral phase based on ref code: 01–077-0341. As can be seen in Fig. 1, after anchoring of Pd, the peak position experiences a shift to a larger angle. It may arise from the generation of stress inside the pristine crystal which changes the cell volume and some crystalline parameters [43]. It is worth noticing that Pd/MoS_2 NHs reveal an additional peak at 2θ = 40.26° corresponding to the 111 crystalline planes of Pd based on the ref code: 00–001-1310. The observed peaks in both samples at 2θ = 33.60° and 33.58° are related to 211 crystalline planes of cubic silicon structure according to ref code: 01–072-1426 and also there are several peaks at about 18.55°, 26.08°, 36.83°, 37.06° and 37.41° corresponding to −101, −111, 200, 111 and 002 planes of MoO_2 structures (ref code: 01–076-1807).

XRD is a powerful technique to probe the interlayer distance in MoS_2

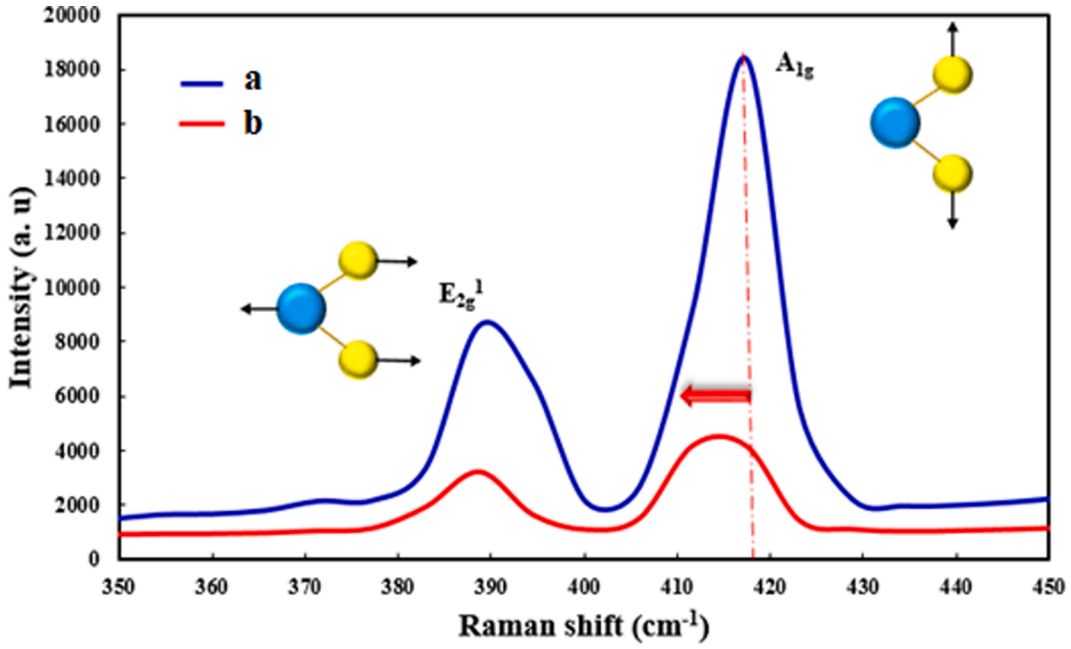

Fig. 4. Raman spectra of a) pristine-MoS_2 NSs and b) Pd/MoS_2 NHs in the range of 350–450 cm^{-1}.

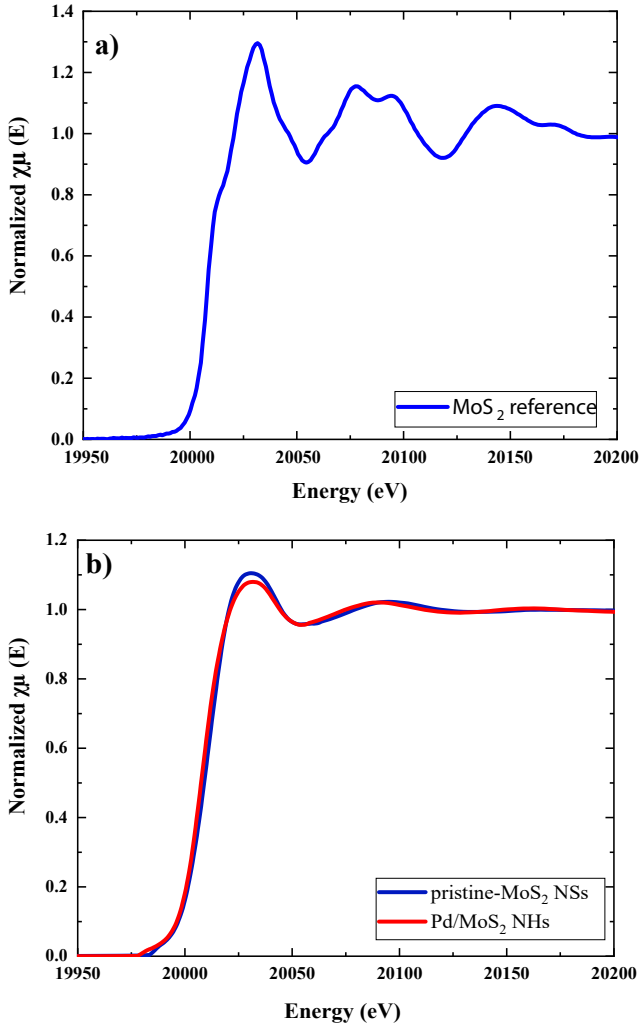

Fig. 5. the normalized absorption spectra in the XANES area for a) MoS_2 reference powder and b) pristine-MoS_2 NSs and Pd/MoS_2 NHs.

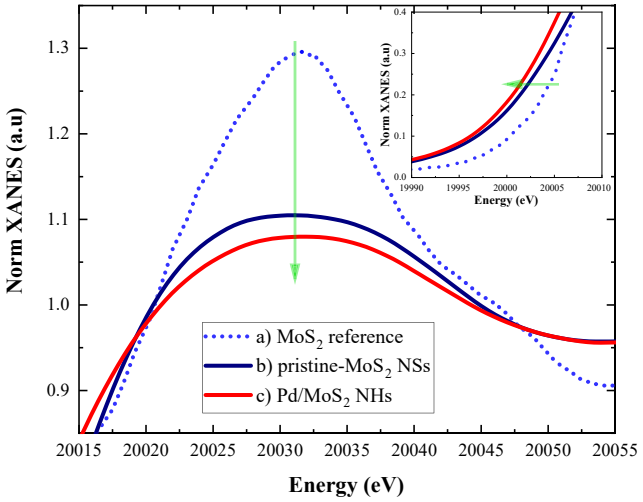

Fig. 6. XANES spectra at Mo K-edge a) MoS_2 reference powder, b) pristine-MoS_2 NSs and c) Pd/MoS_2 NHs; [inset shows Mo K-edge of the samples].

nanostructures [44]. When MoS_2 nanostructure contains multiple MoS_2 molecular layers stacked periodically, it exhibits an XRD pattern with the first two reflection peaks having diploid relationships. According to Bragg's formula: $n\lambda = 2d \sin\theta$. Where n ascertains the diffraction order (for first order n = 1), λ denotes the X-ray wavelength (Cu Kα = 0.15406 Å), d stands for the interplanar distance of lattice in nm and θ represents the Bragg's angle in degree, respectively The d spacing corresponding to the first XRD peak represents the interlayer distance in MoS_2. In this way, by considering the first (003) peak at $2\theta = 14.50^{\circ}$, the interlayer distance for MoS_2 NSs is calculated to be 0.610 nm. Moreover, shifting the first XRD peak to a larger angle indicates a reduction of interlayer distance in the MoS_2 lattice. XRD pattern of Pd/MoS_2 NHs shows the shift of the first (003) peak to 14.59°, corresponding to an interlayer distance of 0.606 nm. Therefore, the results show that the interlayer space reduces due to the Pd entrance in the MoS_2 lattice.

Moreover, the optical properties of the samples are assessed by diffuse reflectance spectrometer. DRS spectroscopy leads to observing

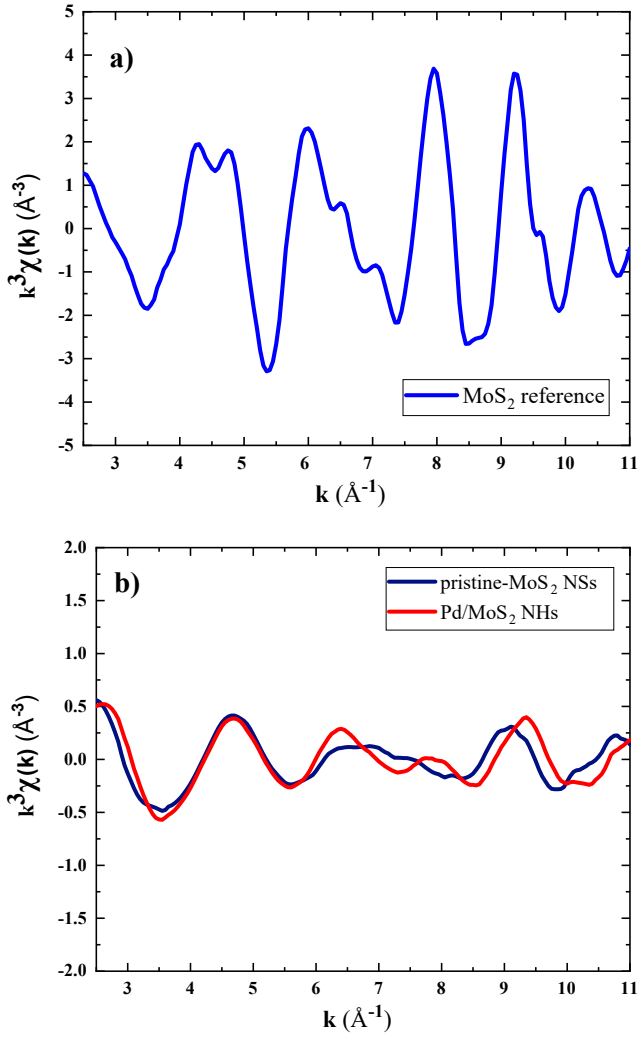

Fig. 7. Mo K edge EXAFS spectra for a) MoS_2 reference powder and b) pristine-MoS_2 NSs and Pd/MoS_2 NHs.

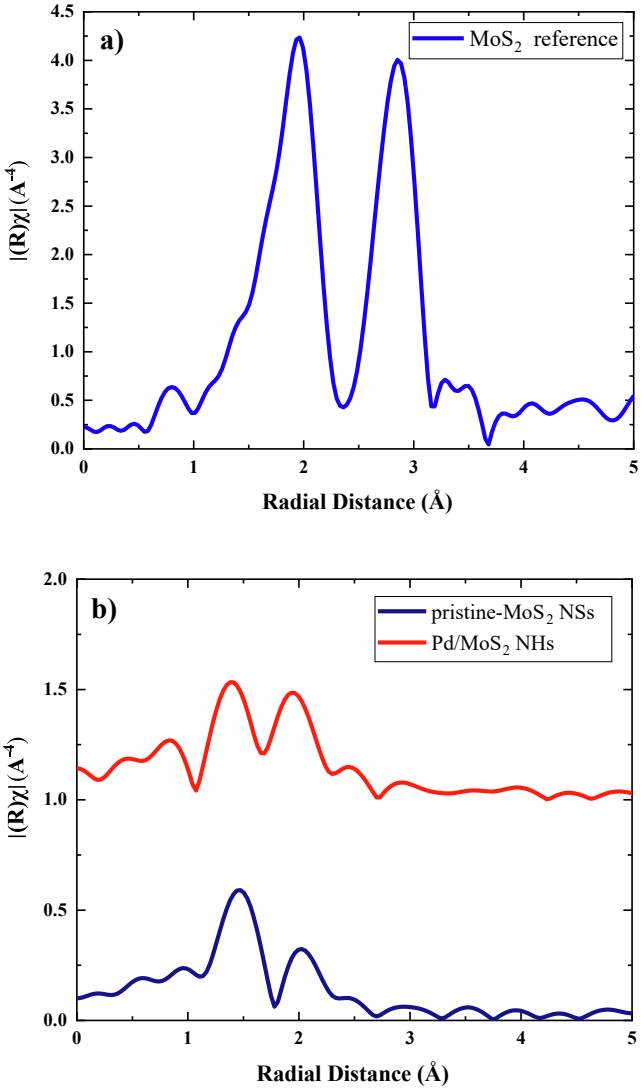

Fig. 8. Radial distribution of Fourier-transformed EXAFS signal for Mo K edge for a) MoS_2 reference powder and b) pristine-MoS_2 NSs and Pd/MoS_2 NHs.

the effect of Pd anchoring on the band gap of the MoS_2 synthesized NSs. The band gap energy of the samples is determined from DRS results using the Kubelka-Munk function [45,46]. Fig. 2 illustrates the reflection spectra of the samples in the wavelength interval range of 300 to 800 nm and the obtained data are tabulated in Table 1. There are obvious valleys attributed to A and B excitons in the spectrum of MoS_2 NSs, while those are weak in Pd/MoS_2 NHs. Moreover, after the Pd anchoring on the MoS_2, these valleys corresponding to A and B excitons experience a redshift of 12.7 and 11 nm, respectively. In addition, the reflection of the sample is enhanced by the Pd anchoring, especially in the region of 500–700 nm wavelength. Furthermore, after Pd anchoring on the MoS_2 semiconductor, the band gap energy slightly decreases to the lower energy at about 0.05 eV.

The absorption of the samples is studied via UV–Visible spectroscopy in the wavelength range of 200–800 nm. Fig. 3 illustrates the absorption spectra of the MoS_2 NSs and Pd/MoS_2 NHs, respectively. As be seen in the corresponded spectra, the absorbance of the MoS_2 enhances in the ultraviolet region after Pd anchoring, while it reduces in the visible area. The discrete surface plasmon absorption in the visible area decreases significantly by Pd anchoring due to a damping effect caused by d–d interband transitions (i.e. the plasmon energy is lost by excitation of single electron interband transitions) [47]. Moreover, the peaks attributing to A and B excitons for MoS_2 NSs appeared at 666 and 605 nm, respectively. After Pd anchoring, A exciton peak has a red shift to a larger wavelength of about 5.5 nm, which can be inferred that there is a direct energy transfer between semiconductor excited states and 3d levels of the Pd ions. Also, due to the existence of various MoS_2 nanoflakes with different layers, one shoulder appeared at 651 nm, which has a redshift to 656 nm after Pd anchoring. The value of Pd metal and MoS_2 semiconductor work function are reported as 5.6 eV and 5.1 eV, respectively [48,49]. The work function difference between Pd and MoS_2 causes electron transfer from MoS_2 into the lower energy states in

Table 2
refined parameter of EXAFS fitting for MoS_2 reference powder, pristine-MoS_2 NSs, and Pd/ MoS_2 NHs.

Sample		2nd Peak (Mo-S)	3rd Peak (Mo-Mo)
Reference	1st Peak (Mo-O)	N_2 R_2 σ_2^2 6.00 2.40 0.0009 2nd Peak (Mo-S)	N_3 R_3 σ_3^2 6.00 3.17 0.0009 3rd Peak (Mo-Mo)
pristine-MoS_2 NSs	N_1 R_1 σ_1^2 1.47 1.99 0.0001 1st Peak (Mo-O)	N_2 R_2 σ_2^2 0.5 2.43 0.0001 2nd Peak (Mo-S)	N_3 R_3 σ_3^2 0.61 3.21 0.006 3rd Peak (Mo-Mo/ Pd)
Pd/ MoS_2 NHs	N_1 R_1 σ_1^2 1.15 1.98 0.0001	N_2 R_2 σ_2^2 0.98 2.40 0.0001	N_3 R_3 σ_3^2 1.79 3.18 0.02

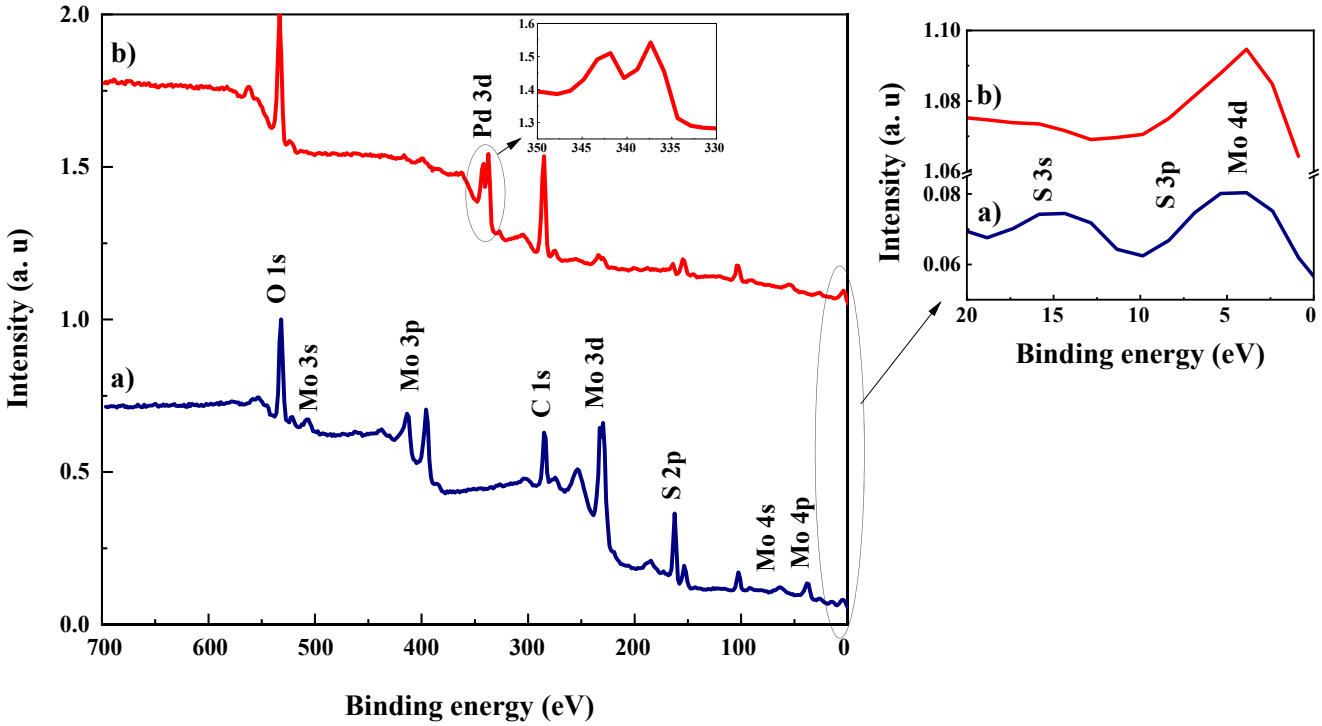

Fig. 9. XPS survey for a) pristine-MoS_2 NSs and b) Pd/MoS_2 NHs.

Table 3
The atomic percentages of the elements in pristine-MoS_2 NSs, and Pd/ MoS_2 NHs.

Sample	Element	Atomic %
pristine-MoS_2 NSs	Mo 3d	38.1
	S 2p	44.2
	O 1 s	17.7
Pd/MoS_2 NHs	Mo 3d	6.4
	S 2p	29.2
	Pd 3d	25.9
	O 1 s	38.5

Pd through a thin interfacial barrier layer and leads to a built-in electric field, directed from MoS_2 toward the Pd metal layer.

Fig. 4 shows the Raman spectra of the MoS_2 NSs and Pd/MoS_2 NHs. The MoS_2 sample exhibits two characteristic Raman peaks, the E^1_{2g} mode at 388.8 cm^{-1} corresponding to the S and Mo atoms oscillating in the antiphase parallel to the crystal plane and the A_{1g} mode at 417.5 cm^{-1} attributing to the S atoms oscillating in the antiphase out-of-plane. According to the figure, the E^1_{2g} peak position almost has no change, while the A_{1g} peak has a redshift of about 5.8 cm^{-1} due to the incorporation of Pd atoms in the MoS_2 nanostructure. The contact between the Pd and MoS_2 NSs can cause enhancement of electron concentration which is responsible for the A_{1g} mode downshift. Moreover, it may arise from the strong binding in Pd/MoS_2 NHs with a clean interface leading to softening of the Mo–S bonds [50]. A_{1g} phonons pair much more firmly with electrons than E^1_{2g} phonons in MoS_2-based substances. So, this indicates that a notable change in the electronic structure and semiconductor characteristics of MoS_2 nanostructure can be caused by Pd anchoring [51]. In addition, the relative intensity of $I_{A_{1g}}$ / $I_{E^1_{2g}}$ decreases after Pd anchoring from 2.1 to 1.3. The most likely phenomena such as strain, defects, grain size, and thickness are known to impact the Raman response, manifesting themselves as changes in peak position, broadening, and intensity that affect the peak ratios [52]. The reduction of the relative intensity of $I_{A_{1g}}$ / $I_{E^1_{2g}}$ can be attributed to layer orientation under the cross-polarized configuration, a transition from a mixed/random grain orientation to a more parallel layered orientation after Pd anchoring on MoS_2 NSs [53].

To study the local structure of the Mo atom and the coordination number, X-ray absorption spectroscopy is carried out at the BL22 - CLÆSS beamline at the Alba Synchrotron, Barcelona, Spain. Several spectra are collected to accumulate them and to have a good enough signal-to-noise ratio. The energy calibration is done using the Mo foil sample and is set to be 20,000 eV at the first maximum above the edge. Fluorescence spectra are obtained at room temperature. The obtained data from EXAFS spectroscopy are analyzed by Demeter software. ATHENA program is applied for data processing including energy calibration, background subtraction, and normalization and the ARTEMIS program is used for data analysis using simulation standards from FEFF standard file. Fig. 5 displays the normalized absorption spectra of MoS_2 reference powder, pristine-MoS_2 NSs, and Pd/MoS_2 NHs. The EXAFS oscillation for both pristine-MoS_2 NSs and Pd/MoS_2 NHs has a reduced amplitude compared with pure MoS_2 powder (MoS_2 reference is prepared from MoS_2 powder), indicating that all samples exhibit weaker short-range order [54].

Fig. 6 shows XANES spectra at Mo K-edge for samples. As can be seen, the white line which is attributed to the first sharp rise in the XANES spectrum and corresponds to transitions of electrons to unfilled bound states just below the continuum of free electron states has decreased for both samples compared to the reference. This decline in the white line confirms a reduction in the unoccupied density of the state of Mo 4d and an average valence state lower than IV [55]. Moreover, in the inset figure, clear differences between the Mo K-edge XANES are evident for pristine-MoS_2 and Pd/MoS_2 samples compared to the MoS_2 reference. The onset of the Mo main absorption gradually shifts to lower energies. This so-called chemical shift reveals a change in the valence state of the incorporated Mo cations [56].

Data are collected from the MoS_2 ref powder before the sample measurements to enable the determination of the amplitude reduction factor (S_0^2), without it the coordination number cannot be identically determined. It is found to be 0.8 and so all coordination numbers and the subsequent results are corrected accordingly. Then, by setting S_0^2 for

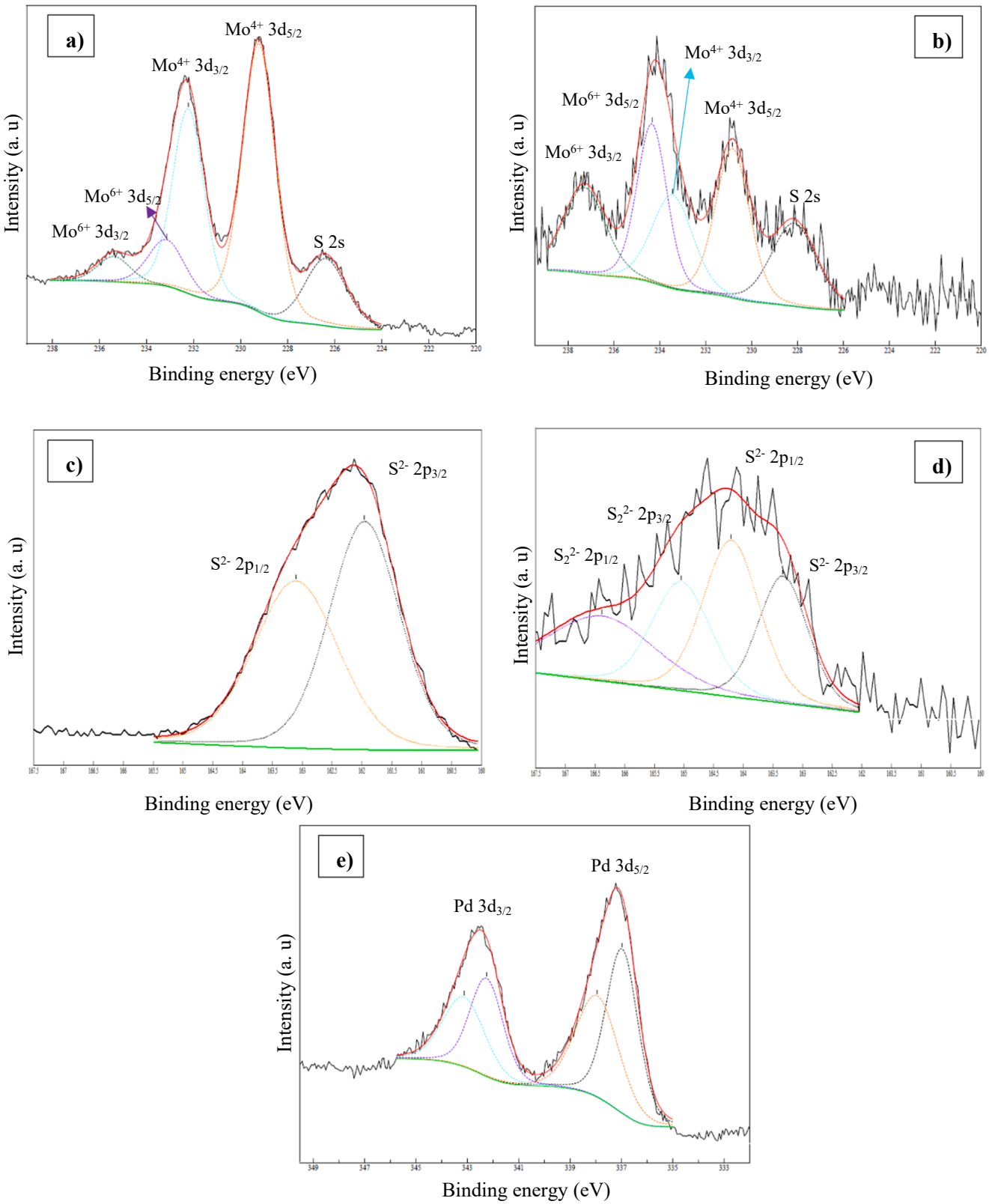

Fig. 10. Deconvoluted XPS spectra of a) and b) Mo 3d, c) and d) S 2p for pristine-MoS_2 NSs and Pd/MoS_2 NHs; e) Pd 3d for Pd/MoS_2 NHs.

each EXAFS data, the Mo-O, Mo-S, and Mo-Mo bond distance, σ^2 parameter, and coordination number are obtained for the samples. The extracted EXAFS spectra and corresponding Fourier transforms for the samples are shown in Figs. 7 and 8. As can be seen in Fig. 7, it is important to notice that, there is a strong difference in the shape of EXAFS oscillations of the samples concerning MoS_2 reference powder. The amplitudes of EXAFS oscillations of the samples are less than the reference powder and also, they have some shifts to different wave-numbers after the Pd anchoring process.

The Fourier transformed of EXAFS spectra are shown in Fig. 8. There

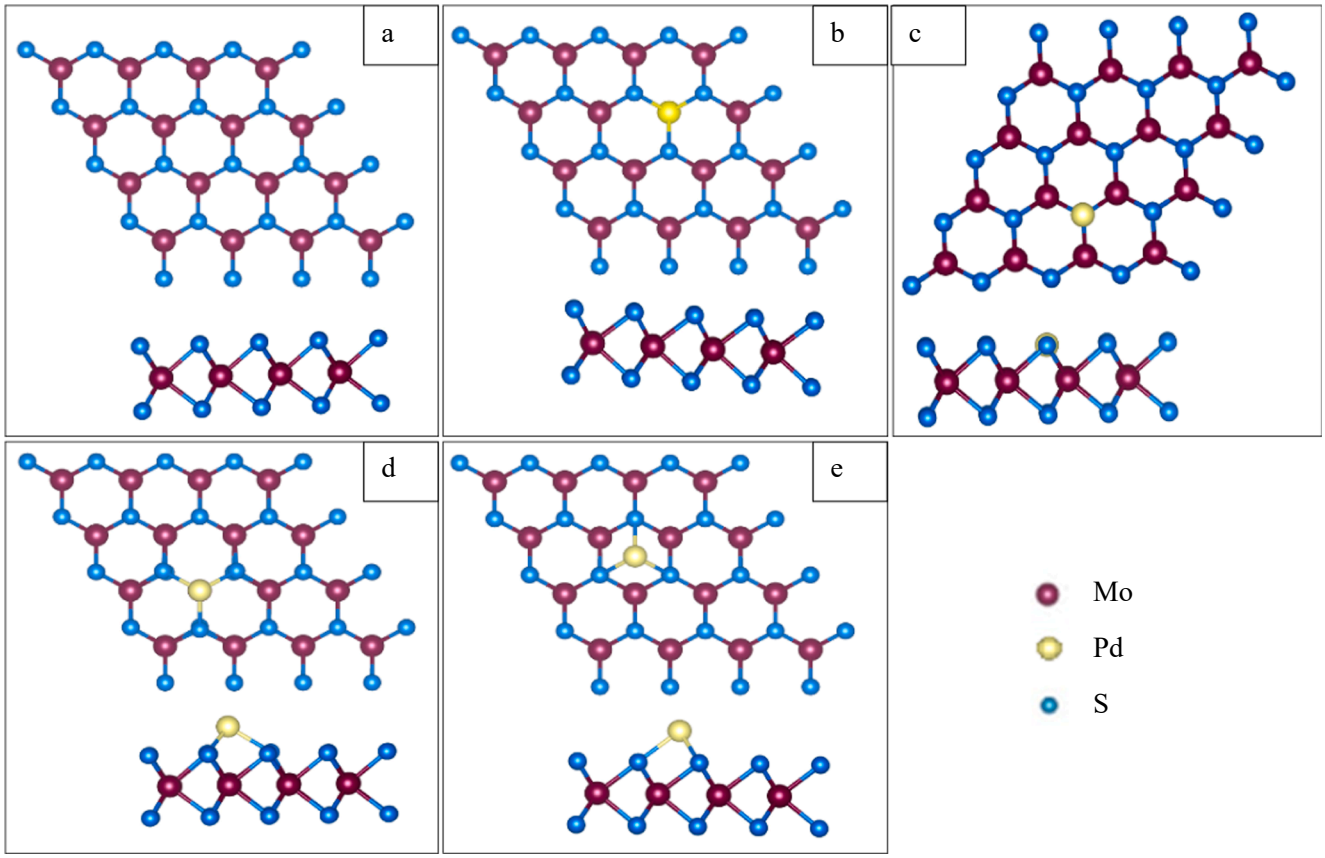

Fig. 11. Side view and up view of the optimized crystalline structure of a) pristine MoS_2, b) Pd atom substitution with a Mo atom, c) Pd atom substitution with an S atom, d) Pd interstitial between Mo and S atoms at the middle bond state and e) Pd interstitial between Mo and S atoms at middle hexagonal state.

Table 4
calculated band gap energy (Eg) and Mo-Mo bond distance for pristine MoS_2 and various modes of Pd- doped on MoS_2.

Simulation information	The calculated band gap (Eg)	Mo-Mo bond distance
Pristine MoS_2	1.767 eV	3.1822 Å
Pd atom substitution with a Mo atom	0.050 eV	3.1822 Å
Pd atom substitution with an S atom	1.288 eV	3.1822 Å
Pd interstitial between Mo and S atoms at middle bond state	1.49 eV	3.1715 Å
Pd interstitial between Mo and S atoms at middle hexagonal state	1.37 eV	3.1933 Å

are three distinct peaks at three radial distances. The first peak corresponds to atomic bonds with O atoms (Mo-O), the nearest neighbor of the transition metal atom (Mo), and the second one is attributed to S atoms (chalcogenides, Mo-S) and the third peak is associated with intralayer cation (transition metal, Mo-Mo) neighbors [17]. Comparison between the spectra of MoS_2 reference and the samples verifies, that there are MoO_2 structures in the samples which are synthesized via the TCVD method. Similarly, the XRD results confirm the presence of MoO_2 in the samples. The fitting consequences for EXAFS data give information about the type, distance, and coordination number of backscatter atoms. As can be seen in Table 2, the first shell for the sample is for Mo-O and second shell is for Mo-S and the third shell is for the Mo-Mo path, respectively [57]. In addition, the changes in Mo-Mo and Mo-O bond distance after Pd anchoring are also extracted by fitting EXAFS. It can be found that due to Pd anchoring on the MoS_2 NSs, the bond distances decrease to smaller values. On the other hand, the Debye-Waller parameter increases after Pd adding due to inducing disorder in the MoS_2 lattice.

The chemical composition and element valence on the surface of MoS_2 NSs and Pd/MoS_2 NHs are analyzed by XPS. As depicted in Fig. 9, the survey spectra confirmed the presentence of Mo, S, and Pd elements. The presence of C and O elements can be observed from the spectra. The O 1 s peak might be caused by the absorbed gaseous molecules and also by molybdenum oxide structures accompanied by the MoS_2 NSs. After Pd anchoring on MoS_2 NSs surface, the intensity of the Mo and S peaks reduces in comparison with the pristine-MoS_2 NSs due to the nature of surface-sensitive XPS analysis. The atomic percentages of O 1 s, Mo 3d, S 2p, and Pd 3d for the samples are presented in Table 3. The corresponding value for O1s increased significantly in Pd/MoS_2 NHs due to the defects created by the plasma effect during Pd anchoring. The deconvoluted XPS spectra of the samples are shown in Fig. 10. In the Mo 3d core-level spectrum (Fig. 10a), the appearance of Mo $3d_{5/2}$ (229.2 eV) and Mo $3d_{3/2}$ (232.2 eV) peaks for Mo 3d doublet indicate the characteristic +4 states [58]. Besides, two weak Mo^{6+} 3d peaks ($3d_{5/2}$ peak at 233.1 eV and $3d_{3/2}$ peak at 235.4 eV) are ascribed to the slight oxidation of MoS_2 NSs. As shown in Fig. 10b, after Pd anchoring Mo^{4+} $3d_{5/2}$, Mo^{4+} $3d_{3/2}$, Mo^{6+} $3d_{5/2}$, and Mo^{6+} $3d_{3/2}$ peaks have shifted to higher binding energy at 230.8, 233.4, 234.3 and 237.3 eV, respectively. It is worth noticing that the Mo^{6+} oxidation peaks intensity has increased after Pd anchoring (Fig. 10a and 10b), while the Mo^{4+} peaks intensity has decreased. This can be attributed to electron transfer from MoS_2 to Pd NPs which is in agreement with our UV–Visible results and also reported by Y. Garcia-Basabe et al. [59].

In the high-resolution scans of S 2p (Fig. 10c), two feature peaks (S $2p_{1/2}$ and S $2p_{3/2}$) appeared at 163.10 and 161.9 eV, respectively, which greatly matched the binding energy of S^{2-} ions in MoS_2. For Pd/MoS_2 NHs, the S 2p (Fig. 10d) region is deconvoluted into two peaks, present at 164.2 eV and 163.3 eV, which are due to the S $2p_{1/2}$ and S $2p_{3/2}$ levels respectively. Differences of 1.2 and 1.4 eV for MoS_2 NSs and Pd/MoS_2

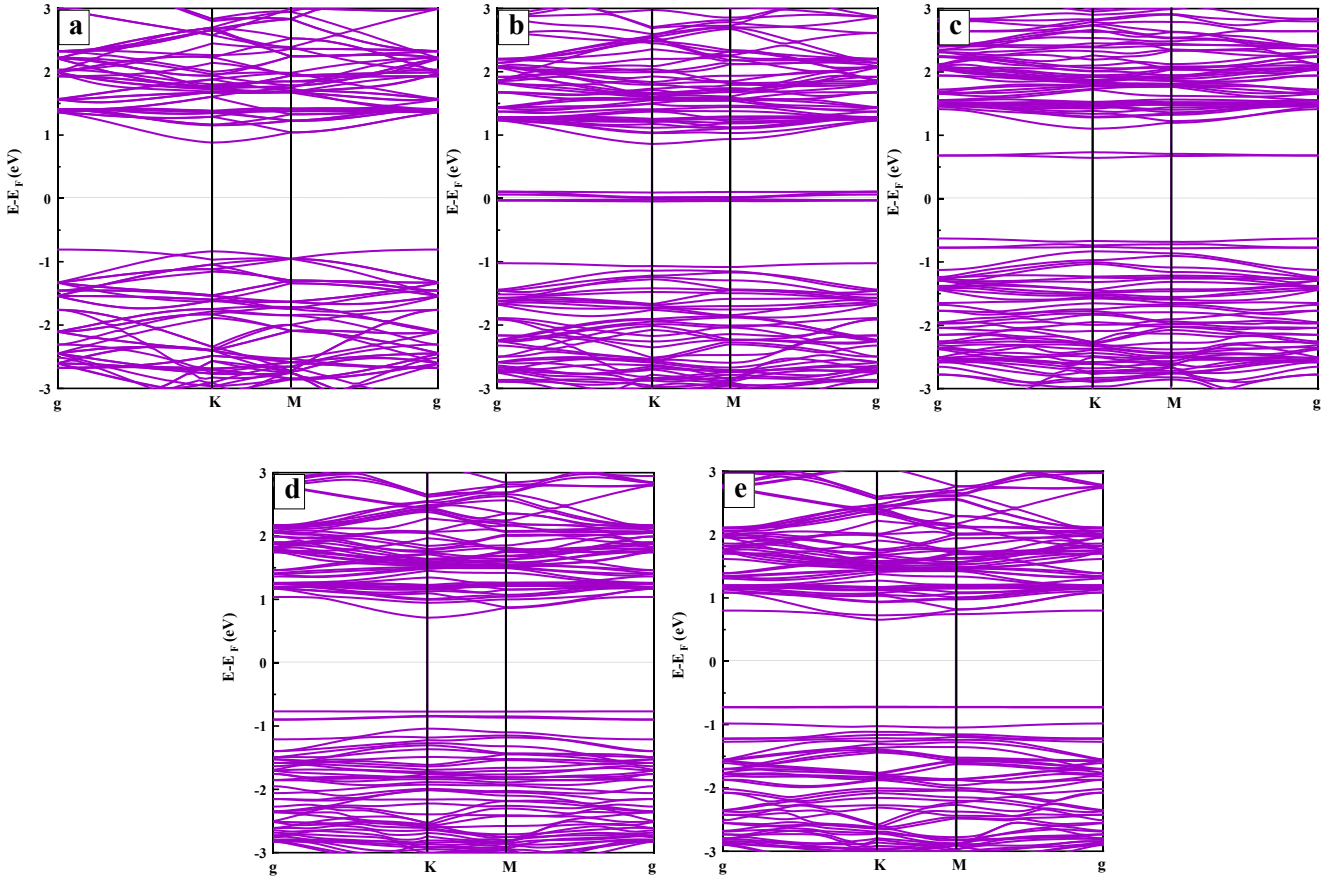

Fig. 12. Calculated band structure of a) pristine MoS_2, b) Pd atom substitution with a Mo atom, c) Pd atom substitution with an S atom, d) Pd interstitial between Mo and S atoms at the middle bond state and e) Pd interstitial between Mo and S atoms at middle hexagonal state.

NHs samples are attributed to the spin–orbit coupling [51,60]. Moreover, new doublet peaks at the higher binding energy at 166.4 and 165.0 eV are corresponding to S_2^{2-} 2p. In the Pd/MoS_2 NHs, Mo 3d and S 2p peaks all shifted to higher binding energies arising from the upshift of the Fermi level toward the conduction band [61,62].

Pd 3d spectrum of the Pd/MoS_2 NHs sample shows two peaks around 336.9 eV and 337.9 eV relating to Pd $3d_{5/2}$ (Fig. 10e) while the peaks at 342.1 eV and 343.0 eV are corresponding to Pd $3d_{3/2}$ levels. A difference of about 5.3 eV is related to the spin–orbit coupling. The binding energy values of pure Pd clusters are reported to be around 335.3 eV and 340.0 eV for $3d_{5/2}$ and $3d_{3/2}$ levels [63,64]. So, the binding energies obtained in this work are much larger than those for metallic Pd and almost the same as the characteristics of Pd^{4+}.

3.1. Simulation result

The electronic band structure calculation of two-dimensional pristine MoS_2 and Pd/ MoS_2 structures is performed using the plane wave basis as implemented in the Quantum Espresso package [65]. The generalized gradient approximation (GGA) in the form of Perdew-BuekeErnzerhof (PBE) is used for the exchange–correlation functional [66]. Ultra-soft method pseudo potentials are chosen for simulations. In all calculations, the kinetic energy cut off is set as 60 Ry for the expansion of plane-wave basis and 10^{-10} Ry as energy convergence thresholds. For the primitive cell relaxation, 12 × 12 × 1 Monkhorst–Pack [67] k-point mesh is used for sampling the Brillouin zone. To prevent the artificial interlayer interaction, a vacuum spacing of 20 Å is considered. Forces convergence thresholds of 10^{-4} Ry per Bohr are selected for geometry structure optimization. To study the effect of Pd adding on the electronic structure of MoS_2, the calculations are carried out for a large 4 × 4 × 1 supercell with 16 Mo atoms and 32 S atoms.

The electronic structure of MoS_2 shows tuneability of band gap with the various modes for placement of Pd atom in the base structure. The top and side views of the MoS_2 structure before and after anchoring are shown in Fig. 11 (a-e) and the simulation results are shown in Table 4. After that, various modes for placement and different sites substitutional doping of Pd atom in MoS_2 structure including a Pd atom replaced a Mo atom at the substitutional site (9b), a Pd atom replaced an S atom at the substitutional site (9c), Pd interstitial between Mo and S atoms in the middle bond state (9d) and Pd interstitial in the middle hexagonal state (9e) are simulated to identify the reasonable place of Pd in MoS_2 structure according to DRS and EXAFS result. The Mo-Mo bond distance has no change after Pd adding on MoS_2 lattice in Pd atom substitution with a Mo atom and Pd atom substitution with an S atom, while in the Pd at Mo and S middle bond state and in the Pd at middle hexagonal state, it has changed to about 3.1715 Å and 3.1933 Å, respectively compared to the Mo-Mo bind distance in the pristine MoS_2 simulation model (3.1822 Å). On the other hand, the refined parameters of EXAFS spectroscopy show a reduction in the Mo-Mo bond distance after Pd anchoring on the MoS_2 structure. Thus, the configuration of Fig. 11d is in agreement with EXAFS results.

Moreover, Fig. 12 illustrates the calculated band structures of all configurations. Note that the valence band maximum and conduction band minimum are both located at the K point of the Brillouin zone, which indicates a direct band gap for all configurations with and without the Pd atom. Furthermore, the electronic band gap experiences a reduction after Pd adding. Due to the DRS result of the samples, the MoS_2 band gap had a slight decrease after the Pd anchoring, which the closest simulation result that confirms this reduction is for the Pd interstitial between Mo and S atoms in Pd at the middle of the bond

state.

4. Conclusion

In this research, molybdenum disulfide nanostructures, MoS_2 NSs, are grown on silicon substrates based on thermal chemical vapor deposition. After that, by using DC magnetron sputtering Pd nanoparticles are anchored on the MoS_2 NSs to form Pd/MoS_2 NHs. XRD, UV–Visible absorption spectroscopy, DRS, Raman, and XPS are carried out to characterize the crystalline structures and optical properties of the samples. The XRD patterns confirm the formation of the rhombohedral crystalline structure phase of MoS_2. Also, it attests to a diffraction peak corresponding to the Pd crystalline plane after Pd anchoring to form Pd/MoS_2 NHs. Moreover, the optical study of the samples indicates a reduction of the absorbance and enhancement of the reflectance after Pd anchoring on MoS_2 NSs in the visible region. The results also show the redshift of A and B excitons and a slight reduction of band gap energy after Pd anchoring. This shift to a larger wavelength can be inferred that there is a direct energy transfer between MoS_2 excited states and 3d levels of the Pd ions. Furthermore, the work function difference between Pd and MoS_2 causes electron transfer from MoS_2 into the lower energy states in Pd through a thin interfacial barrier layer and leads to a built-in electric field, directed from MoS_2 toward the Pd metal layer. Raman results show downshifting of A_{1g} vibration mode due to enhancement of electron concentration by Pd anchoring. Besides that, the reduction of the relative intensity of $I_{A_{1g}}$ / $I_{E^1_{2g}}$ can be related to a more parallel layered orientation after Pd anchoring on MoS_2 NSs. XPS analysis shows electron transfer from Mo 4d electronic states to Pd NPs conduction band. Moreover, after Pd anchoring, all Mo 3d and S 2p peaks have shifted to higher binding energies corresponding to the upshift of the Fermi level toward the conduction band. Also, the binding energies obtained from Pd 3d in Pd/MoS_2 NHs show the characteristics of Pd^{4+}. Moreover, EXAFS spectroscopy is applied to investigate the local structure around the molybdenum K-edge. Mo K-edge for the MoS_2 NSs is investigated using fluorescence mode. In this way, the kind, coordination number, and distance of neighbors of absorber atom are determined. It is found that due to Pd anchoring on the MoS_2 NSs, the bond distances decrease to smaller values. Also, the Debye-Waller parameter increases after Pd adding due to inducing disorder in the MoS_2 lattice. In addition, a simulation study of the structural and electronical properties of the samples is done to understand the effect of Pd adding on MoS_2 structure using Quantum ESPRESSO software. Comparing the simulation results, it is concluded that only for the Pd interstitial between Mo and S atoms at the middle bond state, the Mo-Mo bond distance has decreased. Moreover, the reduction of the band gap after Pd adding has occurred for all simulation models, but the closest model to the experimental results of DRS is the Pd interstitial between Mo and S atoms at the middle bond state.

CRediT authorship contribution statement

A. Taherkhani: Investigation, Data curation, Formal analysis, Writing - original draft. **S.Z. Mortazavi:** Supervision, Conceptualization, Data curation, Investigation, Writing - review & editing. **S. Ahmadi:** Data curation, Software, Formal analysis. **A. Reyhani:** Formal analysis, Investigation, Conceptualization, Data curation.

Declaration of Competing Interest

The authors declare that they have no known competing financial interests or personal relationships that could have appeared to influence the work reported in this paper.

Data availability

No data was used for the research described in the article.

Acknowledgments

The authors gratefully acknowledge the financial support of the Presidential Deputy for Science and Technology, the Institute for Research in Fundamental Sciences, and the Iranian Light Source Facility for the opportunity to be users of the ALBA synchrotron program 2017 (proposal number ID 2017062241). The authors also acknowledge the financial support of the Research Council of Imam Khomeini International University. Furthermore, the authors would like to thank the BL22 CALSS beamline of ALBA Synchrotron, Spain, especially Dr. Carlo Marini for Mo K-edge XAS measurements.

References

[1] H. Cho, D. Kang, Y. Lee, H. Bae, S. Hong, Y. Cho, K. Kim, Y. Yi, J.H. Park, S. Im, Dramatic Reduction of Contact Resistance via Ultrathin LiF in Two-Dimensional MoS2 Field Effect Transistors, Nano Lett. 21 (2021) 3503–3510.
[2] C. Mu, W. Wei, J. Li, B. Huang, Y. Dai, Electronic properties of two-dimensional in-plane heterostructures of WS2/WSe2/MoS2, Mater. Res. Express 5 (2018), 046307.
[3] S. Rashidi, S. Rashidi, R.K. Heydari, S. Esmaeili, N. Tran, D. Thangi, W. Wei, WS2 and MoS2 counter electrode materials for dye-sensitized solar cells, Prog. Photovoltaics Res. Appl. 29 (2021) 238–261.
[4] J. Shao, F. Chen, W. Su, Y. Zeng, H.-W. Lu, Multimodal Nanoscopic Study of Atomic Diffusion and Related Localized Optoelectronic Response of WS2/MoS2 Lateral Heterojunctions, ACS Appl. Mater. Interfaces 13 (2021) 20361–20370.
[5] D.H. Shin, S.H. Shin, S.-H. Choi, Self-powered and flexible perovskite photodiode/solar cell bifunctional devices with MoS2 hole transport layer, Appl. Surf. Sci. 514 (2020), 145880.
[6] M.R. Vazirisereshk, A. Martini, D.A. Strubbe, M.Z. Baykara, Solid lubrication with MoS2: a review, Lubricants 7 (2019) 57.
[7] E.-J. Yu, H.C. Kim, H.J. Kim, S.-Y. Jung, K.-S. Ryu, S.-I. Choi, J.W. Hong, Anisotropic heteronanocrystals of Cu2O–2D MoS2 for efficient visible light driven photocatalysis, Appl. Surf. Sci. 538 (2021), 148159.
[8] H. Zhang, B. Shi, L. Xu, J. Yan, W. Zhao, Z. Zhang, Z. Zhang, J. Lu, Sub-5 nm monolayer MoS2 transistors toward low-power devices, ACS Applied Electronic Materials 3 (2021) 1560–1571.
[9] G. Wang, S. Zhang, X. Zhang, L. Zhang, Y. Cheng, D. Fox, H. Zhang, J.N. Coleman, W.J. Blau, J. Wang, Tunable nonlinear refractive index of two-dimensional MoS 2, WS 2, and MoSe 2 nanosheet dispersions, Photonics Res. 3 (2015) A51–A55.
[10] E. Hoenig, S.E. Strong, M. Wang, J.M. Radhakrishnan, N.J. Zaluzec, J. Skinner, C. Liu, Controlling the structure of MoS2 membranes via covalent functionalization with molecular spacers, Nano Lett. 20 (2020) 7844–7851.
[11] H. Kim, H. Ko, S.M. Kim, H. Rho, Polarization-dependent anisotropic Raman response of CVD-grown vertically stacked MoS2 layers, J. Raman Spectrosc. 51 (2020) 774–780.
[12] M. Annamalai, K. Gopinadhan, S.A. Han, S. Saha, H.J. Park, E.B. Cho, B. Kumar, A. Patra, S.-W. Kim, T. Venkatesan, Surface energy and wettability of van der Waals structures, Nanoscale 8 (2016) 5764–5770.
[13] Y. Kang, Y. Xia, H. Wang, X. Zhang, 2D laminar membranes for selective water and ion transport, Adv. Funct. Mater. 29 (2019) 1902014.
[14] D. Wu, B. Yang, S. Zhang, E. Ruckenstein, H. Chen, Reshaping two-dimensional MoS2 for superior magnesium-ion battery anodes, J. Colloid Interface Sci. 597 (2021) 401–408.
[15] L. Yang, P. Liu, J. Li, B. Xiang, Two-dimensional material molybdenum disulfides as electrocatalysts for hydrogen evolution, Catalysts 7 (2017) 285.
[16] Z. Dong, J. Pan, W. Xiao, J. Wang, C. Li, The MoS2 Quantum Modified Hollow TiO2 Nano-Heterojunction for Enhanced Hydrogen Evolution, in, IOP Conference Series: Earth and Environmental Science, IOP Publishing (2018), 032042.
[17] J. Suh, T.-E. Park, D.-Y. Lin, D. Fu, J. Park, H.J. Jung, Y. Chen, C. Ko, C. Jang, Y. Sun, Doping against the native propensity of MoS2: degenerate hole doping by cation substitution, Nano Lett. 14 (2014) 6976–6982.
[18] D.J. Late, Y.-K. Huang, B. Liu, J. Acharya, S.N. Shirodkar, J. Luo, A. Yan, D. Charles, U.V. Waghmare, V.P. Dravid, Sensing behavior of atomically thin-layered MoS2 transistors, ACS Nano 7 (2013) 4879–4891.
[19] V. Vuong, C. Hung, Direct Synthesis of MoS2 Nanodots by Chemical Vapo r Deposition, Communications in Physics 28 (2018) 379–386.
[20] J. Du, Q. Wang, G. Jiang, C. Xu, C. Zhao, Y. Xiang, Y. Chen, S. Wen, H. Zhang, Ytterbium-doped fiber laser passively mode locked by few-layer Molybdenum Disulfide (MoS2) saturable absorber functioned with evanescent field interaction, Sci. Rep. 4 (2014) 1–7.
[21] X. Fei, Z. Liu, Y. Hou, Y. Li, G. Yang, C. Su, Z. Wang, H. Zhong, Z. Zhuang, Z. Guo, Synthesis of Au NP@ MoS2 quantum dots core@ shell nanocomposites for SERS bio-analysis and label-free bio-imaging, Materials 10 (2017) 650.
[22] F. Haque, T. Daeneke, K. Kalantar-Zadeh, J.Z. Ou, Two-dimensional transition metal oxide and chalcogenide-based photocatalysts, Nano-Micro Letters 10 (2018) 1–27.

[23] X. Ling, Y.-H. Lee, Y. Lin, W. Fang, L. Yu, M.S. Dresselhaus, J. Kong, Role of the seeding promoter in MoS2 growth by chemical vapor deposition, Nano Lett. 14 (2014) 464–472.
[24] V.K. Sangwan, D. Jariwala, I.S. Kim, K.-S. Chen, T.J. Marks, L.J. Lauhon, M. C. Hersam, Gate-tunable memristive phenomena mediated by grain boundaries in single-layer MoS 2, Nat. Nanotechnol. 10 (2015) 403–406.
[25] S. Wang, H. Yu, H. Zhang, A. Wang, M. Zhao, Y. Chen, L. Mei, J. Wang, Broadband few-layer MoS2 saturable absorbers, Adv. Mater. 26 (2014) 3538–3544.
[26] H. Xia, H. Li, C. Lan, C. Li, X. Zhang, S. Zhang, Y. Liu, Ultrafast erbium-doped fiber laser mode-locked by a CVD-grown molybdenum disulfide (MoS 2) saturable absorber, Opt. Express 22 (2014) 17341–17348.
[27] H. Zhang, S. Lu, J.-L. Zheng, J. Du, S. Wen, D. Tang, K. Loh, Molybdenum disulfide (MoS 2) as a broadband saturable absorber for ultra-fast photonics, Opt. Express 22 (2014) 7249–7260.
[28] S. Zu, B. Li, Y. Gong, P.M. Ajayan, Z. Fang, Active control of surface plasmon resonance in MoS2-Ag hybrid nanostructures, arXiv preprint arXiv:1602.04464, (2016).
[29] N.K. Gupta, V. Barwal, L. Pandey, S. Hait, V. Mishra, A. Kumar, S. Chaudhary, Growth of MoS2 by controlled sulfurization of pulsed DC sputtered Mo thin films, in: AIP Conference Proceedings, AIP Publishing LLC, 2020, pp. 090023.
[30] E. Lee, S.G. Lee, W.H. Lee, H.C. Lee, N.N. Nguyen, M.S. Yoo, K. Cho, Direct CVD growth of a graphene/MoS2 heterostructure with interfacial bonding for two-dimensional electronics, Chem. Mater. 32 (2020) 4544–4552.
[31] A. Seynstahl, S. Krauß, E. Bitzek, B. Meyer, B. Merle, S. Tremmel, Microstructure, mechanical properties and tribological behavior of magnetron-sputtered MoS2 solid lubricant coatings deposited under industrial conditions, Coatings 11 (2021) 455.
[32] A. Haghighatzadeh, Enhanced third-order optical susceptibility in Ag-doped CeO2 nanostructures under pulsed Nd-YVO4 laser, Opt. Laser Technol. 126 (2020), 106114.
[33] A. Salah, A.S. Mansour, M. Mohamed, S. Hassab-Elnaby, Nonlinear absorption and optical limiting of Ag–CdSe nano-hybrids of different growth times, Optik 181 (2019) 278–286.
[34] A. Haghighatzadeh, B. Mazinani, Ag/CeO2 Schottky-type nanoheterostructures: Enhanced third-order nonlinear optical susceptibility under the near infrared irradiation, Opt. Laser Technol. 131 (2020), 106426.
[35] A. Sakthisabarimoorthi, S.M.B. Dhas, M. Jose, Fabrication and nonlinear optical investigations of SiO2@ Ag core-shell nanoparticles, Mater. Sci. Semicond. Process. 71 (2017) 69–75.
[36] L. Wu, S. Fang, L. Ge, C. Han, P. Qiu, Y. Xin, Facile synthesis of Ag@ CeO2 core–shell plasmonic photocatalysts with enhanced visible-light photocatalytic performance, J. Hazard. Mater. 300 (2015) 93–103.
[37] M. Ebrahimzadeh, A. Haghighatzadeh, J. Dutta, Improved third-order optical nonlinearities in Ag/MoS2 Schottky-type nano/hetero-junctions, Opt. Laser Technol. 140 (2021), 107092.
[38] G. Bunker, Introduction to XAFS: a practical guide to X-ray absorption fine structure spectroscopy, Cambridge University Press, 2010.
[39] P. Wu, N. Yin, P. Li, W. Cheng, M. Huang, The adsorption and diffusion behavior of noble metal adatoms (Pd, Pt, Cu, Ag and Au) on a MoS 2 monolayer: a first-principles study, PCCP 19 (2017) 20713–20722.
[40] M. Li, J. Yao, X. Wu, S. Zhang, B. Xing, X. Niu, X. Yan, Y. Yu, Y. Liu, Y. Wang, P-type doping in large-area monolayer MoS2 by chemical vapor deposition, ACS Appl. Mater. Interfaces 12 (2020) 6276–6282.
[41] S.-C. Lu, J.-P. Leburton, Electronic structures of defects and magnetic impurities in MoS 2 monolayers, Nanoscale Res. Lett. 9 (2014) 1–9.
[42] V. Selamneni, H. Raghavan, A. Hazra, P. Sahatiya, MoS2/Paper Decorated with Metal Nanoparticles (Au, Pt, and Pd) Based Plasmonic-Enhanced Broadband (Visible-NIR) Flexible Photodetectors, Adv. Mater. Interfaces 8 (2021) 2001988.
[43] R. Karmakar, S. Neogi, A. Banerjee, S. Bandyopadhyay, Structural; morphological; optical and magnetic properties of Mn doped ferromagnetic ZnO thin film, Appl. Surf. Sci. 263 (2012) 671–677.
[44] K.D. Rasamani, F. Alimohammadi, Y. Sun, Interlayer-expanded MoS2, Mater. Today 20 (2017) 83–91.
[45] S.S. Abdullahi, S. Güner, Y. Musa, B.I. Adamu, M.I. Abdulhamid, Sımple method for the determınatıon of band gap of a nanopowdered sample usıng Kubelka Munk theory, NAMP J 35 (2016) 241–246.
[46] A. Belikov, K.Z. Phyo, MoS2 thin films spectrophotometry, in: IOP Conference Series: Materials Science and Engineering, IOP Publishing, 2018, pp. 012008.
[47] M. Khan, M. Al-Oufi, A. Toseef, M. Nadeem, H. Idriss, Comparing the reaction rates of plasmonic (gold) and non-plasmonic (palladium) metal particles in photocatalytic hydrogen production, Catal. Lett. 148 (2018) 1–10.
[48] C. Kim, I. Moon, D. Lee, M.S. Choi, F. Ahmed, S. Nam, Y. Cho, H.-J. Shin, S. Park, W.J. Yoo, Fermi level pinning at electrical metal contacts of monolayer molybdenum dichalcogenides, ACS Nano 11 (2017) 1588–1596.
[49] L. Yang, D. Zhong, J. Zhang, Z. Yan, S. Ge, P. Du, J. Jiang, D. Sun, X. Wu, Z. Fan, Optical properties of metal–molybdenum disulfide hybrid nanosheets and their application for enhanced photocatalytic hydrogen evolution, ACS Nano 8 (2014) 6979–6985.
[50] M. Velicky, A. Rodriguez, M. Bousa, A.V. Krayev, M. Vondracek, J. Honolka, M. Ahmadi, G.E. Donnelly, F. Huang, H.D. Abruna, Strain and charge doping fingerprints of the strong interaction between monolayer MoS2 and gold, The journal of physical chemistry letters 11 (2020) 6112–6118.
[51] L. Hao, W. Gao, Y. Liu, Y. Liu, Z. Han, Q. Xue, J. Zhu, Self-powered broadband, high-detectivity and ultrafast photodetectors based on Pd-MoS 2/Si heterojunctions, PCCP 18 (2016) 1131–1139.
[52] V. Vandalon, A. Sharma, A. Perrotta, B. Schrode, M.A. Verheijen, A.A. Bol, Polarized Raman spectroscopy to elucidate the texture of synthesized MoS 2, Nanoscale 11 (2019) 22860–22870.
[53] M.J. Motala, X. Zhang, P. Kumar, E.F. Oliveira, A. Benton, P. Miesle, R. Rao, P.R. Stevenson, D. Moore, A. Alfieri, Scalable synthesis of 2D van der Waals superlattices, arXiv preprint arXiv:2111.02864, (2021).
[54] J.R. Lince, M.R. Hilton, A.S. Bommannavar, EXAFS of sputter-deposited MoS2 films, Thin Solid Films 264 (1995) 120–134.
[55] Z. Luo, Y. Ouyang, H. Zhang, M. Xiao, J. Ge, Z. Jiang, J. Wang, D. Tang, X. Cao, C. Liu, Chemically activating MoS2 via spontaneous atomic palladium interfacial doping towards efficient hydrogen evolution, Nat. Commun. 9 (2018) 1–8.
[56] B. Henne, V. Ney, K. Ollefs, F. Wilhelm, A. Rogalev, A. Ney, Magnetic interactions in the Zn-Co-O system: tuning local structure, valence and carrier type from extremely Co doped ZnO to ZnCo2O4, Sci. Rep. 5 (2015) 1–8.
[57] Y.V. Zubavichus, A. Golub, Y.N. Novikov, Y.L. Slovokhotov, A. Nesmeyanov, P. Schilling, R. Tittsworth, XAFS study of MoS2 intercalation compounds, Le Journal de Physique IV, 7 (1997) C2-1057-C1052-1059.
[58] J. Wang, X. Feng, D. Hedman, X. Wu, H. Pan, Q. Zhang, Enhancing the hydrogen evolution reaction on MoS2 flakes by cold plasma treatment, Electrochem. Commun. 137 (2022), 107250.
[59] Y. Garcia-Basabe, G.F. Peixoto, D. Grasseschi, E.C. Romani, F.C. Vicentin, C. E. Villegas, A.R. Rocha, D.G. Larrude, Phase transition and electronic structure investigation of MoS2-reduced graphene oxide nanocomposite decorated with Au nanoparticles, Nanotechnology 30 (2019), 475707.
[60] S. Huang, Z. You, Y. Jiang, F. Zhang, K. Liu, Y. Liu, X. Chen, Y. Lv, Fabrication of ultrathin MoS2 nanosheets and application on adsorption of organic pollutants and heavy metals, Processes 8 (2020) 504.
[61] Q. Deng, X. Li, H. Si, J. Hong, S. Wang, Q. Feng, C.X. Hu, S. Wang, H.L. Zhang, K. Suenaga, Strong Band Bowing Effects and Distinctive Optoelectronic Properties of 2H and 1T′ Phase-Tunable MoxRe1–xS2 Alloys, Adv. Funct. Mater. 30 (2020) 2003264.
[62] J. Gao, Y.D. Kim, L. Liang, J.C. Idrobo, P. Chow, J. Tan, B. Li, L. Li, B.G. Sumpter, T. M. Lu, Transition-metal substitution doping in synthetic atomically thin semiconductors, Adv. Mater. 28 (2016) 9735–9743.
[63] R. Bhatt, S. Bhattacharya, R. Basu, A. Singh, U. Deshpande, C. Surger, S. Basu, D. Aswal, S. Gupta, Growth of Pd4S, PdS and PdS2 films by controlled sulfurization of sputtered Pd on native oxide of Si, Thin Solid Films 539 (2013) 41–46.
[64] S. Sarkar, S. Sampath, Equiatomic ternary chalcogenide: PdPS and its reduced graphene oxide composite for efficient electrocatalytic hydrogen evolution, Chem. Commun. 50 (2014) 7359–7362.
[65] P. Giannozzi, S. Baroni, N. Bonini, M. Calandra, R. Car, C. Cavazzoni, D. Ceresoli, G.L. Chiarotti, M. Cococcioni, I. Dabo, QUANTUM ESPRESSO: a modular and open-source software project for quantum simulations of materials, J. Phys.: Condens. Matter 21 (2009), 395502.
[66] J.P. Perdew, K. Burke, M. Ernzerhof, Generalized gradient approximation made simple, Phys. Rev. Lett. 77 (1996) 3865.
[67] H.J. Monkhorst, J.D. Pack, Special points for Brillouin-zone integrations, Physical review B 13 (1976) 5188.